Tailoring Ag/g-C_3N_4/TiO_2 Nanocomposites via Distinct Synthesis Routes for Enhanced Photocatalytic Degradation of Reactive Red 4 Dye

Nur Hidayatul Syazwani Suhaimi[1], Nur Syamimi Adzis[1], Rahil Azhar[1], Muhammad Zahiruddin Ramli[2], Mohd Yusof Hamzah[3], Wan Izhan Nawawi[1]* and Mohd Azlan Mohd Ishak[1]

[1]Photocatalysis Laboratory, Faculty of Applied Sciences, Universiti Teknologi MARA Cawangan Perlis, 02600 Arau, Perlis, Malaysia

[2]Faculty of Chemical Engineering, Universiti Teknologi MARA Cawangan Pulau Pinang, 13500 Permatang Pauh, Pulau Pinang, Malaysia

[3]Radiation Processing Division, Malaysian Nuclear Agency, 43000 Kajang, Selangor, Malaysia

*Corresponding author (e-mail: wi_nawawi@uitm.edu.my)

Heterogeneous photocatalysis is one of the most extensively studied approaches in mitigating the issue of wastewater pollution. The synthesis method of photocatalytic materials significantly affects their properties and performance. In this study, g-C_3N_4/TiO_2 nanocomposites were synthesised through three different preparation methods: dry solid-state (D), wet solid-state (W), and *in situ* solvothermal synthesis (S), and were consequently modified with Ag nanoparticles to exploit its surface plasmon resonance (SPR) effect. Ag/g-C_3N_4/TiO_2 prepared using the wet solid-state method (A_3WTC) showed impressive photocatalytic efficiency for RR4 dye degradation with a rate of 0.1052 min^{-1}. The enhancement is attributed to its improved photocatalytic properties, including small average crystallite size of 8.76 nm, particle size of 18.2 nm, lower bandgap energy of 2.69 eV, and lower electron-hole recombination rate. This comparative study sheds light on the effect of various g-C_3N_4/TiO_2 synthesis methods and the effectiveness of Ag doping on the photocatalytic performance of the nanocomposites in the photodegradation of RR4 dye. The findings contribute to the development of efficient and sustainable photocatalytic materials for environmental remediation applications.

Keywords: Titanium dioxide; graphitic carbon nitride; silver; synthesis routes; photodegradation; water treatment

Received: March 2025; Accepted: June 2025

Industrial effluent is a major contributor to global water pollution. An estimated 359 billion cubic metres of wastewater is produced annually on a global scale, with Malaysia contributing approximately 2.97 billion cubic metres of industrial effluent [1]. As of 2008, Malaysia ranked as the fifteenth largest textile fibre producer worldwide and ninth in Asia [2]. The elevated wastewater discharge from the textile industry positions it as one of the major contributors to water pollution in Malaysia, where it accounts for 22% of the country's total industrial wastewater. The textile industry consumes large quantities of organic dyes, particularly during the colouring and dyeing processes. However, inefficiencies in the dyeing process result in significant dye loss, ranging from 20% to 50%, which are often discarded with wastewater into nearby water bodies. Among various types of dyes, azo dyes are particularly recalcitrant, non-biodegradable, and persistent in the environment [3].

Reactive Red 4 (RR4), also known as Cibacron Brilliant Red, is a widely used synthetic organic azo dye with the molecular formula $C_{32}H_{23}ClN_8O_{14}S_4$ and a molecular weight of 995.23 g mol^{-1}. It contains reactive groups like sulfonic acid (-SO_3H) and chlorine (-Cl), allowing it to bond strongly to textile fibres. Due to its strong binding ability, RR4 exhibits excellent wash, light fastness, and bleach resistance characteristics, making it ideal for application in the textile industry [4]. However, its chemical structure, which consists of two azo groups (-N=N-) attached to benzene rings, renders it highly carcinogenic and mutagenic. The presence of such dye in untreated wastewater can trigger public concerns due to its potential health risks. It also poses significant environmental and public health risks if discharged untreated into natural water bodies. Therefore, the development of efficient wastewater treatment methods is essential to eliminate these harmful dye molecules and other organic contaminants, contributing to a cleaner and safer environment.

Among the myriad remediation strategies, photocatalysis using semiconductor materials is lauded

for its high efficiency, environmentally friendly, and cost-effectiveness compared to other conventional methods like adsorption, filtration, flocculation, biological, physical, and chemical treatment methods [5]. Photocatalysis focuses on the formation of highly reactive oxygen species (ROS) such as hydroxyl radicals (•OH) and superoxide anions (O_2•$^-$) through redox reactions. These ROS are useful to degrade primarily organic chemical pollutants into harmless substances like water (H_2O) and carbon dioxide (CO_2) [6]. •OH radical is particularly potent due to its high oxidation potential (~2.8 eV) and non-selective nature, giving it the capability to degrade a wide range of organic compounds. In photocatalysis, semiconductor photocatalysts are activated by photon absorption, causing the electrons (e^-) to be excited from the valence band (VB) to the conduction band (CB), leaving behind positively charged holes (h^+). These photogenerated charge carriers enable simultaneous oxidation and reduction reactions, where electrons reduce oxygen molecules and holes oxidise water or hydroxide ions to produce ROS [7]. Equations 1-5 and Figure 1 summarise the photocatalytic mechanism occurring in an activated photocatalyst. Several well-known semiconductors for photocatalytic purposes include titanium dioxide (TiO_2), zinc oxide (ZnO), tungsten trioxide (WO_3), cadmium sulphide (CdS), and graphitic carbon nitride (g-C_3N_4).

$$\text{Photocatalyst} + h\nu \rightarrow e^- + h^+ \quad (1)$$

$$O_2 + e^- \rightarrow \bullet O_2\text{-} \quad (2)$$

$$\bullet O_2^- + H_2O \rightarrow HO_2\bullet \quad (3)$$

$$H_2O / OH^- + h+ \rightarrow \bullet OH \quad (4)$$

$$\text{Organic pollutants} + \bullet O_2^- / HO_2\bullet / \bullet OH \rightarrow CO_2 + H_2O \quad (5)$$

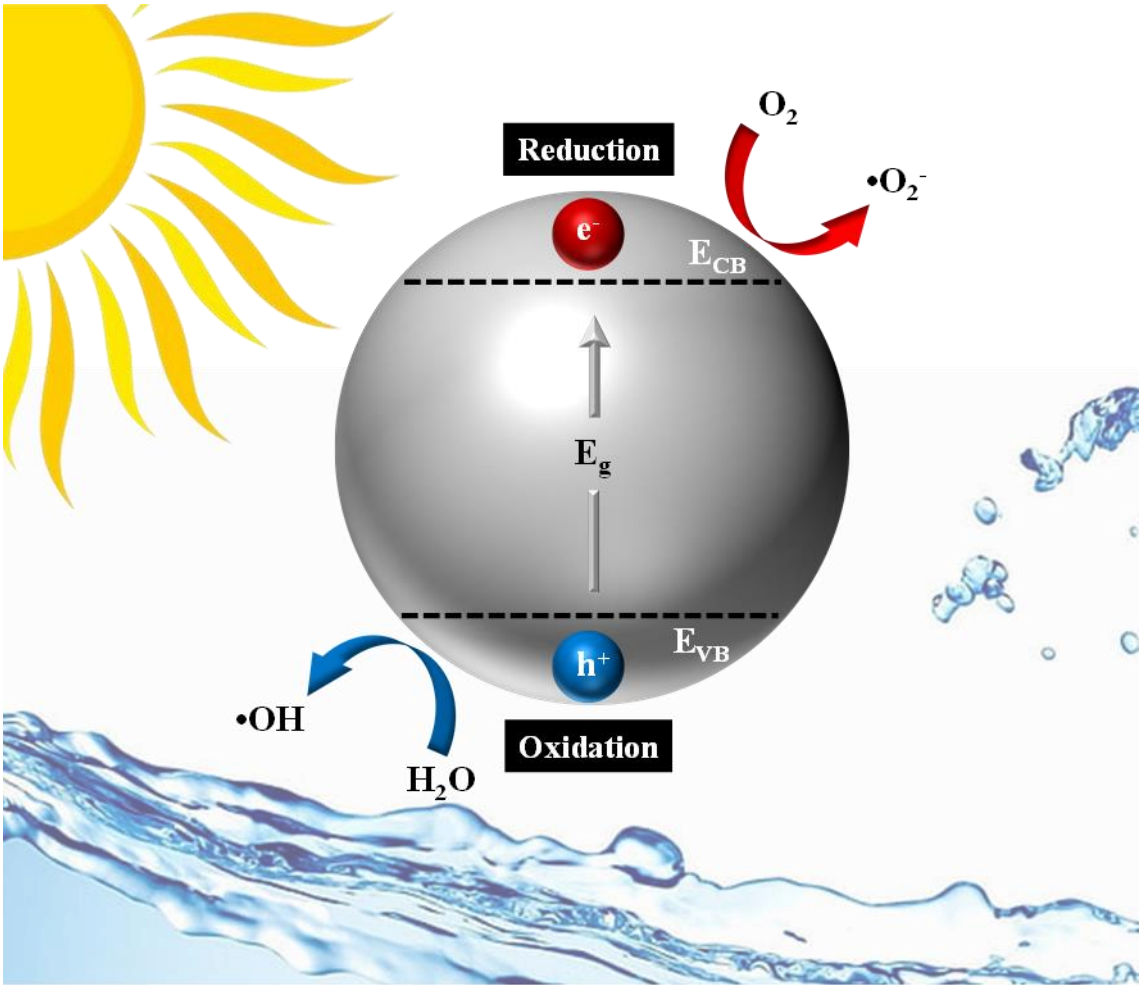

Figure 1. The proposed photocatalytic mechanism of a semiconductor photocatalyst.

Anatase titanium dioxide (TiO_2) is one of the most common semiconductors used as a heterogeneous photocatalyst in wastewater treatment. Despite its high activity and stability, TiO_2 photocatalytic performance is still restricted by the wide band gap (3.2 eV) and fast recombination of photogenerated charge carriers [8]. Coupling different semiconductors to form heterojunctions is one of the efficient techniques to improve photocatalytic activity. In this context, graphitic carbon nitride (g-C_3N_4) has been gaining a lot of interest in the wastewater treatment area as a promising metal-free semiconductor photocatalyst due to its efficient band gap (2.7 eV) and easy production [9]. The combination of TiO_2 and g-C_3N_4 was found to demonstrate highly enhanced photocatalytic activity towards organic pollutants under visible light [10,11]. It is mostly ascribed to the broadening of the light absorption spectrum and the formation of a heterojunction between the two semiconductors, which effectively separates the photogenerated electrons and holes, leading to enhanced photocatalytic performance. As an instance, TiO_2-g-C_3N_4 synthesised by Saeed et al. [12] exhibited better photocatalytic performance compared to pure TiO_2 and g-C_3N_4 for sunlight-assisted photodegradation of Congo red dye. UV-Vis DRS revealed that the band gap for the TiO_2-g-C_3N_4 was 2.94 eV, enhancing the composite's ability to absorb light in the visible region. Besides, the heterojunction formed at the interface of TiO_2 and g-C_3N_4 facilitates charge separation, resulting in higher production of ROS for photodegradation process. Figure 2 illustrates the surge in research literature on g-C_3N_4/TiO_2 photocatalysts in recent years, indicating their growing popularity.

Researchers have been studying and developing various methods to synthesise g-C_3N_4/TiO_2 nanocomposites. Among them, solid-state and solvothermal preparation approaches are commonly performed due to their ability to produce well-defined and controlled morphology with enhanced properties. The solid-state method, typically involving calcination or heat treatment at very high temperatures, promotes crystallisation and improves structural properties of photocatalysts, particularly for metal oxide semiconductors [13]. However, this process may reduce the surface hydroxyl groups and specific surface area due to sintering and crystal growth [14]. In contrast, solvothermal synthesis facilitates crystal growth in a solvent at relatively low temperatures, allowing precise tuning of the photocatalyst's properties by adjusting the experimental parameters, such as solvothermal temperature, duration, pressure, type of solvent and many others [15]. These methods yield the same nanocomposites with different photocatalytic properties and performance [16-18]. Each synthesis route significantly influences the photocatalytic behaviour of resulting composites, regulating their reactivity or selectivity through distinct modifications of their morphological, structural, optical, and electronic properties, as supported by Albiter et al. [19]. These variations originate from unique molecular interactions that occur during synthesis, highlighting the importance of investigating and optimising these synthesis routes in order to obtain highly functional and efficient photocatalysts.

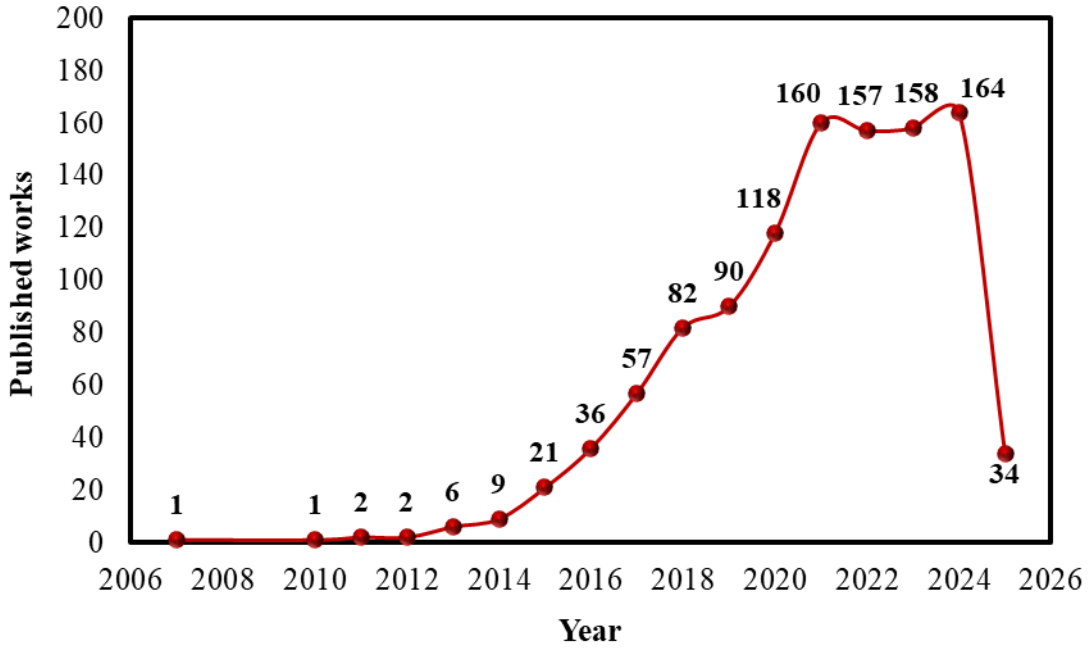

Figure 2. The number of scholarly works published on g-C_3N_4/TiO_2 photocatalysts with "g-C_3N_4/TiO_2 " and "Photocatalysis" as keywords from 2006 to 2025, as reported on "lens.org".

Building on these findings, this study explores the photocatalytic properties of Ag/g-C_3N_4/TiO_2 nanocomposites, where the g-C_3N_4/TiO_2 hybrids were prepared using three different approaches: dry solid-state, wet solid-state, and in situ solvothermal methods. Through advanced characterisation analyses, this study provides insights into the influence of synthesis methods on the photocatalytic properties of the resulting nanocomposites. Ag was incorporated in the nanocomposites to further enhance their photocatalytic performance through the formation of Schottky barrier and SPR effect for visible light absorption [20]. Gan et al. [21] reported on an Ag-doped TiO_2/g-C_3N_4 photocatalyst prepared via a simple chemical reduction reaction. The absorption edge of the ternary Ag/TiO_2/g-C_3N_4 experienced a significant red shift compared to the binary TiO_2/g-C_3N_4, signalling that the SPR effect of Ag improved the nanocomposite's visible light absorption. Furthermore, the construction of the ternary heterojunction photocatalyst facilitated charge carrier separation and retarded recombination process, as evidenced by its high photocurrent density and lower photoluminescence emission peak compared to the binary and pure materials. These synergistic effects led to enhanced removal of tetracycline hydrochloride with Ag/TiO_2/g-C_3N_4 showing the degradation rates 1.91, 1.63, and 1.31 times higher than those of TiO_2, g-C_3N_4, and TiO_2/g-C_3N_4, respectively. In this study, the efficiency of modified Ag-doped photocatalysts was evaluated through the photodegradation of RR4 dye under visible light irradiation to highlight the critical role of synthesis routes in optimising photocatalytic activity.

EXPERIMENTAL

Chemicals and Materials

Titanium(IV) isopropoxide ($(Ti(OCH(CH_3)_2)_4)$), urea ($(CO(NH_2)_2$, Pur. 99%), silver nitrate ($AgNO_3$), 95% ethanol, and reactive red 4 (RR4) dye (model pollutant) were purchased from Sigma Aldrich. Distilled water was used throughout this study.

Preparation of Anatase TiO_2

Anatase TiO_2 was first prepared using a solvothermal method with titanium(IV) isopropoxide (TTIP) as the TiO_2 precursor. TTIP was dissolved in ethanol under a stirring condition for 60 minutes with the ratio of TTIP to ethanol of 3:7. The mixture was then transferred to a Teflon autoclave reactor and heated at 180ºC for 8 hours. After 8 hours, the product was centrifuged and dried overnight. The product was ground into fine powder.

Preparation of g-C_3N_4

g-C_3N_4 was prepared using urea as the precursor. Approximately 20 g of urea was placed inside a crucible and combusted at 550ºC for 30 minutes with a heating rate of 5ºC/min. The obtained pale yellow powder was lightly ground and transferred into a screw-capped bottle for further uses.

Preparation of g-C_3N_4/TiO_2 using Dry Solid-State Approach

The synthesis of g-C_3N_4/TiO_2 nanocomposites was carried out following a previously reported dry solid-state method by Fagan et al. [18] with minor adjustments. The prepared g-C_3N_4 was physically mixed with anatase TiO_2 and calcined in a closed crucible at 450°C for 30 minutes with a heating rate of 5°C/min. The ratio of g-C_3N_4 to TiO_2 was 3:7. The final product was ground annotated as DTC.

Preparation of g-C_3N_4/TiO_2 using Wet Solid-State Approach

The procedure for the wet solid-state approach of g-C_3N_4/TiO_2 was almost similar to the dry solid-state approach method except that g-C_3N_4 and TiO_2 were mixed in the presence of ethanol, in which a paste was formed. The paste was then compressed in a closed crucible and calcined at 450°C for 30 minutes with a heating rate of 5°C/min. The final product was ground annotated as WTC.

Preparation of g-C_3N_4/TiO_2 using *in situ* Solvothermal Approach

The preparation was similar to the preparation of solvothermal anatase TiO_2 but with the addition of g-C_3N_4 during the stirring step. The solvothermal process took place for 8 hours at 180°C in an electric oven. Then, the product was cooled at room temperature and washed with 70% ethanol and distilled water. The residue was dried overnight at 80°C and ground into fine powder (g-C_3N_4/TiO_2). STC was used as the acronym for the sample of the *in situ* preparation.

Preparation of Ag/g-C_3N_4/TiO_2 using Photodeposition Method

After the formation of optimised g-C_3N_4/TiO_2 nanocomposites, Ag was deposited on their surfaces via photodeposition method as described by Shokri et al.[10], with slight adjustments. In this study, $AgNO_3$ solution was used as the Ag precursor, with the Ag concentration of 300 ppm. Inside a Schlenk tube, 0.3 g of a prepared g-C_3N_4/TiO_2 nanocomposite was poured into 12 mL of 50% isopropyl alcohol. $AgNO_3$ was added into the tube and the mixture was mixed until homogeneous. The air inside the tube was removed using a vacuum pump and nitrogen gas was purged into the tube. The slurry was left for 5 hours for the soaking process to take place. Next, the slurry was irradiated with a 250 W metal halide lamp for 60 minutes under a stirring condition. The product was centrifuged at 6000 rpm for 10 minutes and washed

with distilled water at least twice. Finally, the precipitate was left to dry at room temperature overnight. A_3DTC, A_3WTC, and A_3STC represented the Ag-doped g-C_3N_4/TiO_2 nanocomposites prepared through dry solid-state, wet solid-state, and *in situ* solvothermal syntheses, respectively.

Characterisation Methods

X-ray diffraction analysis (XRD) is very important in order to identify the crystalline phases present in the prepared Ag/g-C_3N_4/TiO_2 samples along with their crystallinity and phase purity. The samples were investigated using powder X-ray diffraction on a Bruker D8 Advance diffractometer at 2θ angle in the range of 5° to 80° with a step size increment of 1.00/step and a scan speed of 5 deg/min.

The modified samples were subjected to this UV-Vis Diffuse Reflectance Spectroscopy (UV-Vis DRS) analysis to study their UV-Vis absorbance trend and the shifting in the band gap energy. A Shimadzu UV-Vis spectrophotometer using barium sulphate ($BaSO_4$) as a reference standard was utilised.

FTIR was utilised to characterise newly generated bonds, as well as to verify and identify known and unknown bonds or functional groups in the synthesised samples. In this investigation, about 0.1 g of sample was subjected to Fourier Transform Infrared - Attenuated Total Reflectance (FTIR-ATR) analysis to assess the functional groups and bondings in the samples. The FTIR spectra were collected in a wider wavenumber range from 4000 to 600 cm^{-1}.

FESEM analysis was conducted to further study the morphology of the modified samples. For this analysis, the samples were ground and sieved using an Endecotts Ltd sieve with a 150 μm aperture size to acquire fine catalyst particles. The samples were then coated with gold and examined using a LEO 1530 field emission scanning electron microscope (FESEM) operated at 3 kV. The composition of the samples was quantified using EDX analysis simultaneously.

Photoluminescence (PL) spectroscopy was mainly employed to analyse the separation of photogenerated electron-hole since the signal produced is the result of carrier recombination. For this analysis, approximately 0.1 g of the sample materials was turned into pellets inside the sample holder. The samples were analysed using a Perkin Elmer LS55 fluorescence spectrophotometer, with an excitation wavelength at 324 nm, to study the properties of the active sites and comprehend the surface processes of the modified samples.

Photocatalytic Study

The photocatalytic efficiency of the prepared Ag/g-C_3N_4/TiO_2 was evaluated based on the procedure reported by Abdul Ghani et al. [22], with slight modifications. The study was done based on the photodegradation of 25 mL of 30 mg L^{-1} RR4 dye under the irradiation of a 55 W fluorescent lamp and the catalyst loading of 0.0313 g. RR4 dye was set to have a constant neutral pH. An aquarium pump model NS 7200 was used as an aeration source to supply sufficient oxygen during the photodegradation process. The aeration flowrate was fixed at 70 mL min^{-1} throughout the process. Absorbance values were measured with a HACH DR 1900 spectrophotometer, at the wavelength of 517 nm, to determine the remaining percentage of dye after the photocatalytic degradation process. The remaining percentage of dye was calculated using the formula shown in Equation 1 below. In this formula, C_o and C_t refer to the initial and final RR4 concentrations, respectively.

$$Percentage\ remaining\ (\%) = \frac{C_o - C_t}{C_o} \times 100\% \quad (1)$$

RESULTS AND DISCUSSION

The XRD diffractograms of the modified samples (Figure 3a) demonstrated the successful formation of anatase TiO_2, as indicated by the characteristic peaks that correspond with the Bragg reflections of the standard bulk TiO_2 crystallised in the anatase phase (JCPDS card 21-1272) [23]. The g-C_3N_4 component exhibited two prominent diffraction peaks at 11.8º and 27.7º, corresponding to the (100) and (002) planes of g-C_3N_4 (JCPDS card 87–1526), indicating that g-C_3N_4 was successfully synthesised [24]. However, these peaks were absent in the Ag/g-C_3N_4/TiO_2 spectra, which may have been due to the lower ratio of g-C_3N_4 to TiO_2 (30:70) in the nanocomposites [25]. No peaks related to metallic Ag^0 were observed in the diffractograms of A_3DTC and A_3STC, which may have resulted from the high Ag nanoparticle dispersion within the TiO_2 and g-C_3N_4 matrix or could indicate that the Ag nanoparticles were in an amorphous state [26]. In contrast, the diffractogram of A_3WTC exhibited an additional peak at 38.1º, which aligns with the (200) Bragg reflection of Ag with a face-centred cubic structure (space group Fm3m, JCPDS card 04-0783) [27]. It suggests the successful Ag photodeposition on the nanocomposite surfaces and the reduction of Ag^+ to metallic Ag^0. For further justification, the lattice parameter of Ag(200) plane was calculated based on the lattice formula for a cubic system using the formula shown in Equation 2, with *hkl* representing the Miller indices. The formed Ag nanoparticles exhibited a lattice parameter of 4.06 Å, aligning closely with the standard value for metallic face-centred cubic Ag (4.09 Å) [28]. The findings suggest that g-C_3N_4/TiO_2 synthesised through the wet solid-state method possesses a structure conducive to the formation of more crystalline Ag nanoparticles compared to those prepared via the dry solid-state and *in situ* solvothermal methods.

$$Lattice\ parameter, \alpha = d_{hkl}\sqrt{h^2 + k^2 + l^2} \quad (2)$$

The average crystallite size of TiO_2 in the Ag-doped nanocomposites was determined using the Sherrer's formula, as shown in Equation 3. This formula considers the radiation wavelength (λ) (specifically λ = 1.5406 Å for CuKα) and the full width at half maximum (FWHM) of peaks (β) measured in radians at any 2θ position within the diffractogram. K in the formula represents the shape factors of the crystalline particles, influenced by both non-instrumental and instrumental factors, with a widely accepted numerical value of 0.9 [29]. The calculated TiO_2 crystallite size and their respective crystallinity index are presented in Table 1. All synthesised Ag-doped materials possessed nano-sized crystalline particles ranging from 6 to 10 nm, and in the following order: A_3STC > A_3WTC > A_3DTC. Meanwhile, A_3WTC exhibited the highest crystallinity index at 84.20%, followed by A_3STC (78.14%) and A_3DTC (76.75%).

$$Crystallite\ size, D_{hkl} = \frac{K\lambda}{\beta_{hkl}\cos\theta} \quad (3)$$

The FTIR spectrum (Figure 3b) of TiO_2 showed a characteristic band at 611 nm, which indicates Ti-O-Ti stretching vibration. Meanwhile, the peak in the region between 1250 to 1650 nm in g-C_3N_4 spectrum corresponds to the stretching and rotational vibration of C-N and C-NH bonds. The broad band observed at 3000 to 3400 nm in the same spectra corresponds to the stretching modes of N-H groups. A sharp peak observed at approximately 800 nm indicates the bending vibration of heptazine rings [30,31]. These characteristic peaks were also present in the spectra of the Ag/g-C_3N_4/TiO_2 nanocomposites, though with varying intensities, confirming the successful incorporation of both TiO_2 and g-C_3N_4 into the composites without significant disruption of their chemical structures during the coupling and Ag deposition processes.

Table 1. Crystallinity index and crystallite size of synthesised photocatalysts.

	A_3DTC	**A_3WTC**	**A_3STC**
Crystallinity index, %	76.75	84.20	78.14
Crystallite size, nm	6.25	8.76	9.71

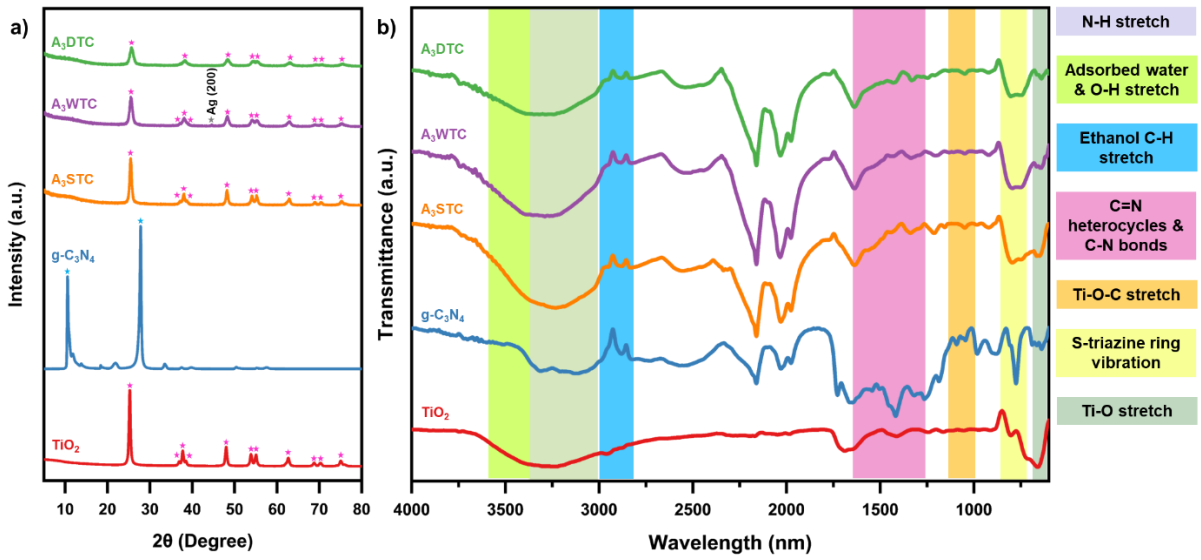

Figure 3. (a) XRD diffractogram and (b) FTIR spectra of TiO_2, g-C_3N_4, A_3DTC, A_3WTC, and A_3STC nanocomposites.

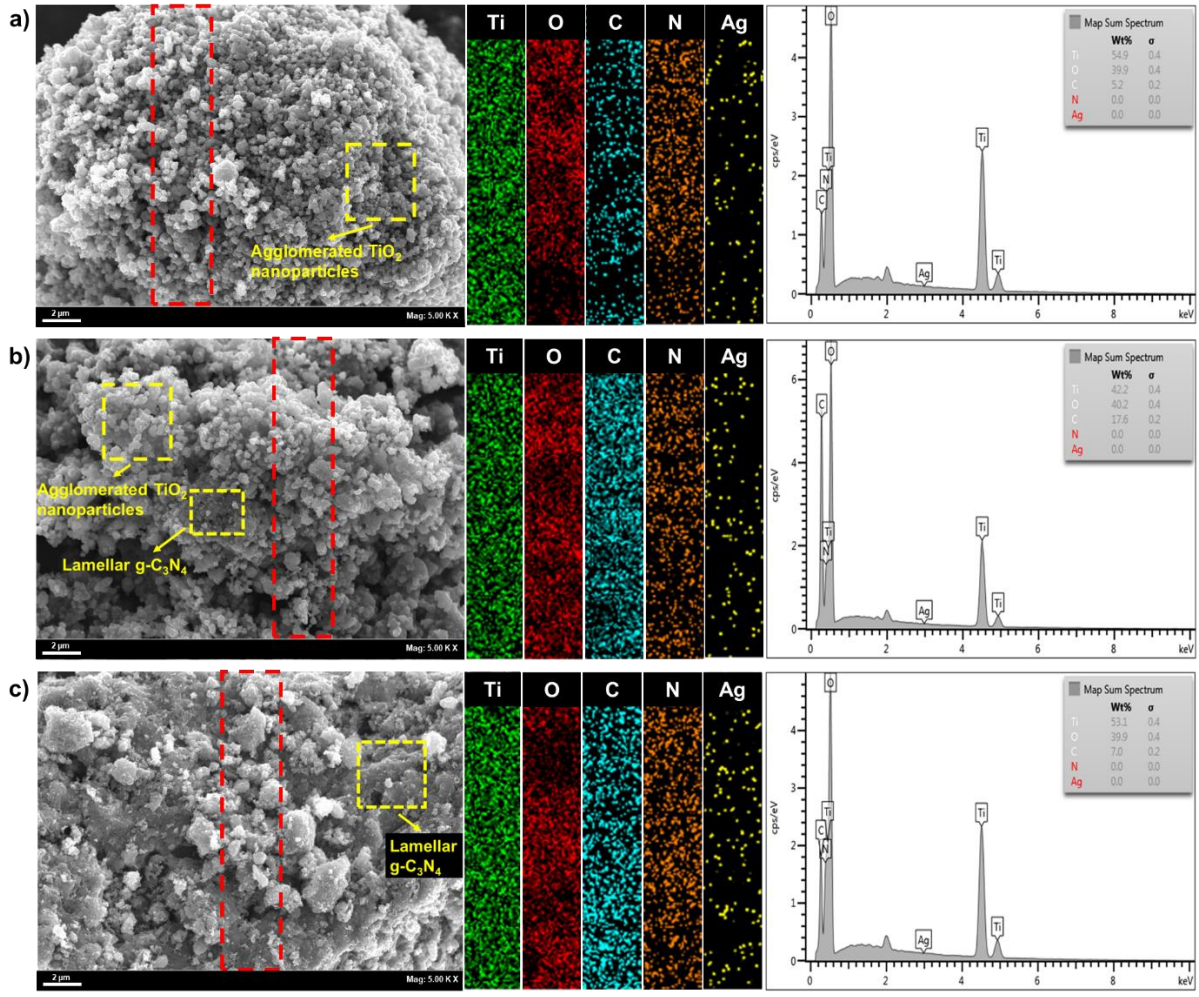

Figure 4. FESEM images, elemental mapping, and EDX analysis of (a) A_3DTC, (b) A_3WTC, and (c) A_3STC nanocomposites.

FESEM images (Figure 4) revealed distinct structural features of the semiconductors, with TiO_2 appearing spherical and g-C_3N_4 displaying irregular lamellar structure. The surfaces of A_3DTC and A_3WTC were dominated by TiO_2, while g-C_3N_4 was predominant on the surface of A_3STC. The difference in surface dominance is the result from the methods used to synthesise g-C_3N_4/TiO_2 materials. In the solid-state preparation method, the calcination process enhances the crystallinity of TiO_2 and promotes particle aggregation. During aggregation, TiO_2 particles form larger clusters that eventually cover the g-C_3N_4 structure [32]. Figures 4a and 4b show that TiO_2 nanoparticles with sizes of 22.7 and 18.2 nm aggregated into larger particles, reaching 318.1 and 272.7 nm, respectively. In contrast, the *in situ* solvothermal process employed for A_3STC synthesis (Figure 4c) facilitates interlayer delamination of g-C_3N_4, leading to a uniform distribution throughout the composite photocatalyst [16]. This process may lead to the TiO_2 being covered by the delaminated g-C_3N_4 layers, making the g-C_3N_4 sheets the dominant surface structure. The presence of Ag could not be confirmed from the FESEM images alone as the nanoparticles were too small to be visually discernible [22,33]. Thus, elemental mapping and EDX analysis were performed. Elemental mapping depicted a relatively uniform distribution of Ag in all three nanocomposites. However, due to very low percentage of Ag loading and its potentially high dispersion or ultrafine particle size, which most likely fell below the detection threshold of the instrument, no distinct peak related to Ag appeared in the EDX spectra. Nonetheless, the uniform mapping signal supports the inferred presence of Ag in the nanocomposites. Meanwhile, the weight percentage (wt%) of N appeared as 0 in the EDX spectra. It may be attributed to the proximity of the characteristic X-ray energy of N (Kα = 0.392 eV) to that of Ti (Lα = 0.452 eV), which can result in peak overlap and hinder accurate elemental quantification [34].

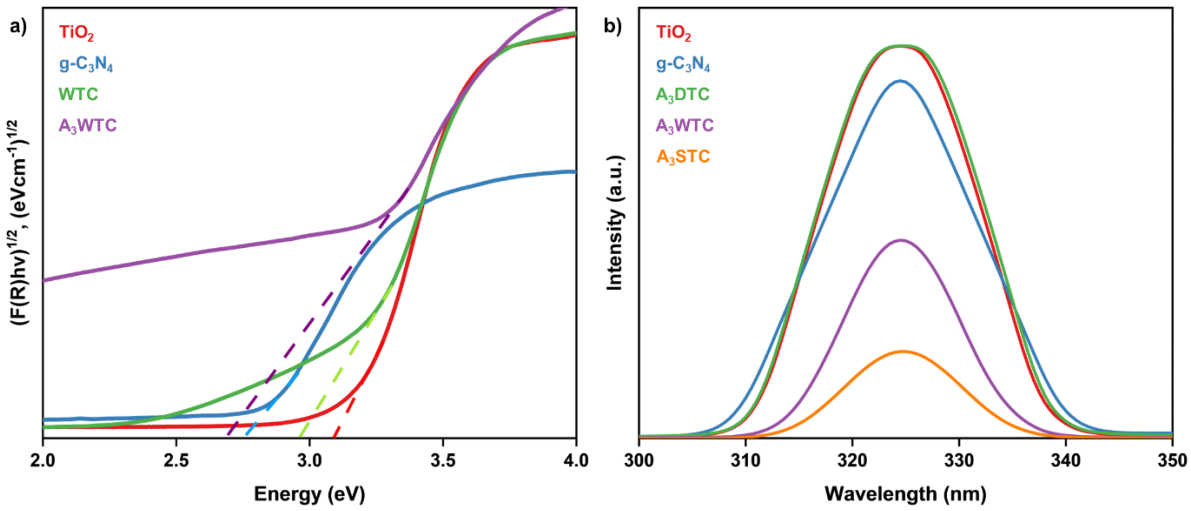

Figure 5. (a) Tauc plot and (b) PL spectra of synthesised photocatalysts.

The UV-Vis DRS analysis was performed to examine the band gap and light absorption abilities of the synthesised g-C_3N_4, TiO_2, WTC, and A_3WTC. WTC and A_3WTC were chosen as the representative samples among the binary and ternary nanocomposites for detailed optical characterisation due to their optimum photocatalytic efficiency towards RR4 degradation compared to their counterparts. The band gap energy (E_g) of the samples was determined based on the absorption data and calculated using the Tauc's equation, as given in Equation 4; where α, h, v, n, and A represent the absorption coefficient, Planck's constant, light frequency, and constant, respectively [35].

$$(\alpha h\upsilon)^n = A(h\upsilon - E_g) \quad (4)$$

Based on the Tauc's equation, a Kubelka-Munk function plot was plotted as $(F(R)hv)^{1/2}$ against energy of light, as shown in Figure 5a. The observed band gap energies of TiO_2, g-C_3N_4, WTC, and A_3WTC were 3.10, 2.75, 2.95, and 2.69 eV, respectively. The reduction in band gap energy in WTC compared to pristine TiO_2 can be attributed to the introduction of g-C_3N_4, which possesses lower band gap energy, into the nanocomposite. Band gap reduction allows nanocomposites to effectively absorb light at longer wavelengths; in this case, specifically within the visible spectrum. This enhanced light absorption promotes the generation of photogenerated electron-hole pairs, which plays a critical role in facilitating redox reactions and increasing the production of ROS, crucial for efficient pollutant degradation [22,35]. The incorporation of Ag nanoparticles into the WTC nanocomposite further boosted the reduction of the band gap energy to 2.70 eV. It is most likely ascribed to the SPR effect exhibited by Ag nanoparticles. The SPR effect exhibited by noble metal nanoparticles can lead to the broadening of the light absorption range, consequently reducing the band gap energy of a photocatalyst [36].

The PL spectra of pristine and Ag-doped samples were analysed and compared in Figure 5b. A weaker PL peak intensity corresponds to a low recombination rate of photogenerated electron-hole pairs, thus extending the lifetime of these charge carriers, which typically results in enhanced photocatalytic performance [37]. Pristine TiO_2 and g-C_3N_4 displayed intense PL peaks, suggesting that the semiconductors experienced a rapid charge carrier recombination rate. The emission signal of A_3DTC was comparable to that of pristine TiO_2. This result may be caused by Ag acting as a recombination centre for the electron-hole pairs, leading to a higher charge recombination rate and stronger peak intensity [38]. In contrast, A_3WTC and A_3STC displayed improved charge separation, as observed by the reduced emission intensity. The findings indicate that Ag can effectively retard the electron-hole recombination by creating a Schottky junction, which traps and retains the excited electrons for a duration, thus reducing recombination rates and enhancing carrier lifetimes [39,40]. The recombination rate in A_3STC may be further reduced due to the delaminating g-C_3N_4 acting as a passivating layer, which reduces the surface defect sites within the nanocomposite, where recombination typically occurs [31,41,42].

The photocatalytic efficiency of the prepared Ag/g-C_3N_4/TiO_2 was determined based on the photodegradation of 25 mL of 30 mg L^{-1} RR4 dye under the irradiation of a 55 W fluorescent lamp irradiation and the catalyst loading of 0.0313 g. The findings indicate that the RR4 degradation follows a pseudo-first-order kinetic process since a good correlation for the fitted lines was obtained with R^2

values greater than 0.95 (Figure 6a) [43, 44]. Figures 6b and 6c showcase the percentage of remaining RR4 dye and the photodegradation rates for the synthesised photocatalysts, respectively. Notably, A_3WTC demonstrated a better RR4 photodegradation rate than pristine TiO_2 and g-C_3N_4, with a rate constant of 0.1052 min^{-1}. This significant enhancement is ascribed to the wet solid-state synthesis that produced g-C_3N_4/TiO_2 with properties that allow Ag nanoparticles to effectively form crystallites. The crystallite Ag nanoparticles exhibited a strong SPR effect, which broadened the light spectrum, simultaneously lowering the band gap energy for better absorption of visible light. Furthermore, crystalline Ag nanoparticles possess the ability to form a Schottky barrier at the metal-semiconductor junction. This barrier traps photogenerated electrons, inhibiting their recombination with holes and prolonging the charge carrier lifetimes for the reaction with the pollutant. The improved charge utilisation leads to enhanced photocatalytic activity. A_3WTC also possessed high crystallinity (84.2%) with smaller crystallite (8.76 nm) and particle size (18.2 nm), providing the photocatalyst with a larger surface area and abundant active sites for the pollutant to be adsorbed and degraded.

A_3DTC showed only a slight improvement in terms of the RR4 degradation rate compared to TiO_2. It might be due to the Ag existing in an amorphous state, as evidenced by the absence of Ag crystalline peaks in the XRD diffractogram. Amorphous Ag lacks the well-defined ordered structure found in crystalline metals, which limits its ability to exhibit a strong SPR effect [45-47]. This reduction in SPR effect restricted the activity of A_3DTC under visible light irradiation, thus decreasing the degradation of RR4 dye. Furthermore, amorphous Ag might also act as a recombination centre, further reducing the photocatalytic performance. The amorphous nature of Ag may also contribute to the poor photocatalytic performance of A_3STC (0.0475 min^{-1}), which demonstrated a poor photodegradation rate than the pristine semiconductors. Additionally, although the delaminated layer of g-C_3N4 in A_3STC contributed to the reduction of charge recombination, it also created a physical barrier between pollutant molecules and TiO_2 nanoparticles, significantly limiting the interaction and charge transfer between them. Furthermore, the dominant layer of bulk g-C_3N_4 on the surface resulted in a lower specific surface area, thus further impairing its photocatalytic performance [48,49].

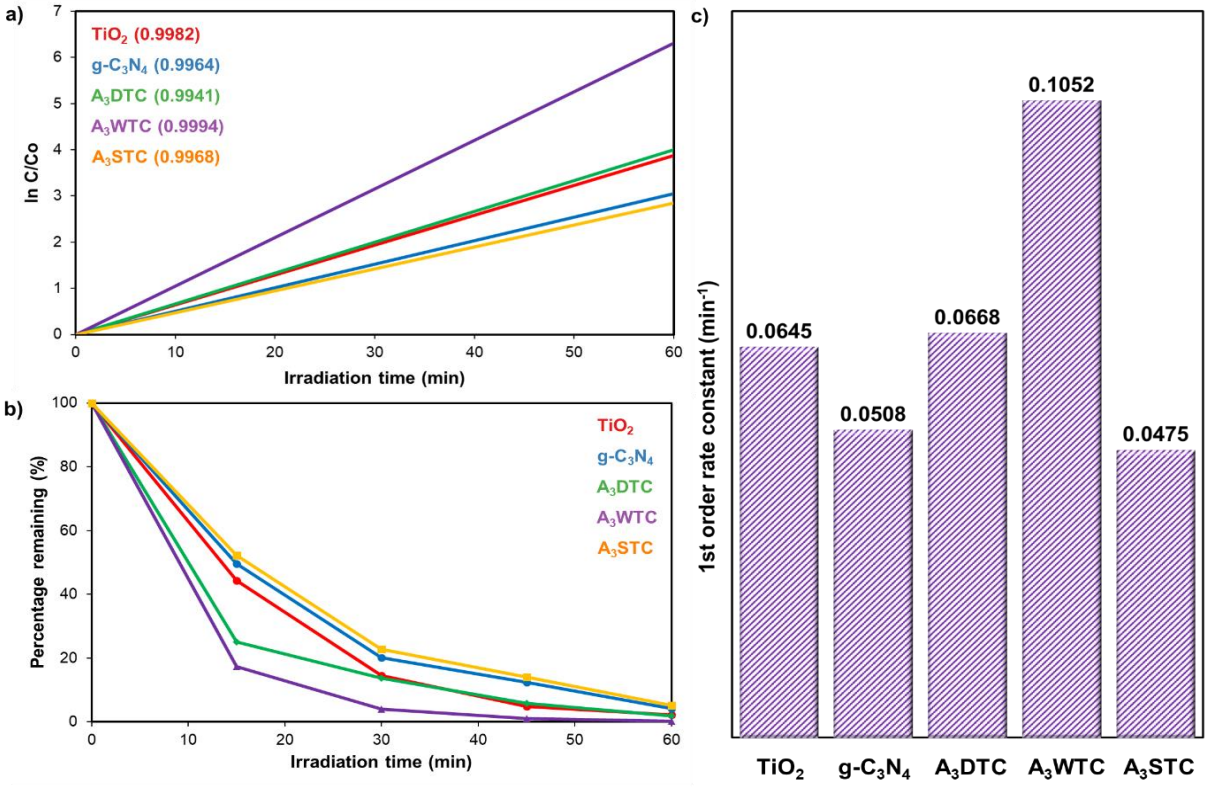

Figure 6. (a) Pseudo-first-order kinetic plot, (b) percentage of remaining dye within 60 minutes of irradiation, and (c) photodegradation rate of 30 mg L^{-1} RR4 dye using synthesised photocatalysts.

Table 2. The comparison of the photodegradation of organic dyes by Ag/g-C_3N_4/TiO_2 photocatalysts.

Sample	**Reaction condition**	**Dyes**	**K (min^{-1})**	**Ref**
A_3WCT	[RR4] = 30 ppm $M_{catalyst}$ = 0.0313 g 50 W fluorescent lamp	RR4	0.1052	This work
2CN:1ST	[RhB] = 10 ppm [MO] = 10 ppm $M_{catalyst}$ = 50 mg 120 mW/cm^2 visible light	RhB, MO	RhB = 98.13% MO = 92.82% degraded within 30 min	[50]
TCA	[R6G] = 10^{-1} M $M_{catalyst}$ = 1 x 2 cm^2, 3 mg 300 W xenon lamp	R6G	64.9% degraded within 100 min	[51]
Ag/g-C_3N_4/TiO_2	[RhB] = 10 ppm $M_{catalyst}$ = 20 mg 300 W xenon lamp	RhB	0.046	[52]
CNAT	[Tartrazine] = 10 ppm $M_{catalyst}$ = 30 mg 300 W xenon lamp	Tartrazine	0.01143	[53]

The optimal Ag/g-C_3N_4/TiO_2 nanocomposite (A_3WTC) prepared in this work exhibited a superior photocatalytic activity in terms of dye degradation compared to previous studies, as shown in Table 2.

CONCLUSION

This study demonstrated the successful synthesis and characterisation of TiO_2-based nanocomposites (g-C_3N_4/TiO_2) modified with Ag nanoparticles for enhanced photocatalytic degradation of RR4 dye. The results reveal that the preparation method plays a crucial role in determining photocatalytic efficiency, with the wet solid-state preparation of g-C_3N_4/TiO_2 yielding the most efficient nanocomposite. The small crystallite (8.76 nm) and particle size (18.2 nm) of the A_3WTC nanocomposite contributed to the enhanced specific surface area and active sites for photocatalytic reaction to occur on the surface. Additionally, the presence of crystalline Ag nanoparticles boosted the photocatalytic activity by exhibiting an SPR effect and forming a Schottky barrier, which resulted in the reduction of the band gap energy (2.69 eV), effective utilisation of visible light, and better charge carrier separation. In conclusion, this study highlights the potential of Ag/g-C_3N_4/TiO_2 nanocomposites for improved photocatalytic applications, emphasising the importance of synthesis method to maximise photocatalytic efficiency. These findings contribute to the development of more efficient and sustainable photocatalysts for environmental remediation.

LIMITATIONS AND FUTURE OUTLOOKS

While the study demonstrates the successful synthesis of Ag/g-C_3N_4/TiO_2 nanocomposites via distinct routes and their promising performance in RR4 dye degradation, several limitations remain. Firstly, the optical and structural characterisation were limited to selected samples (e.g., UV-Vis DRS was conducted only for WTC), which restricts full comparison across all synthesis methods. Secondly, the low loading of Ag made it difficult to detect and confirm its presence conclusively via EDX and XRD, and advanced techniques such as XPS or HRTEM were not employed due to resource constraints. Thirdly, the study focused only on RR4 dye under controlled laboratory conditions without evaluating real wastewater or a range of pollutants.

Future research should explore a broader range of synthesis parameters to further optimise photocatalyst performance. Comprehensive characterisation, including XPS, HRTEM, and PL spectroscopy, would offer deeper insights into the charge transfer dynamics and chemical states of the elements involved. Expanding the scope to include degradation of mixed or real wastewater samples, along with reusability and long-term stability assessments, would also enhance the practical relevance of the materials. Furthermore, mechanistic studies involving active species trapping and kinetic modelling could provide a more detailed understanding of the degradation pathways.

ACKNOWLEDGEMENT

The authors would like to extend the acknowledgment and gratitude to Ministry of Higher Education (MOHE) for providing the generous financial support under Fundamental Research Grants Scheme (FRGS) 2024: 600-RMC/FRGS 5/3 (088/2024).

REFERENCES

1. Tuan Mat, E. A., Shaari, J. & Voon, K. H. (2011) Wastewater production, treatment, and use in Malaysia. *UN-Water*.

2. Ahmad, S. S., Mulyadi, I. M. M., Ibrahim, N. & Othman, A. S. (2016) The application of recycled textile and innovative spatial design strategies for a recycling centre exhibition space. *Procedia - Social and Behavioral Sciences*, **234**, 525–535.

3. Selvaraj, V., Karthika, T. S., Mansiya, C. & Alagar, M. (2020) An over review on recently developed techniques, mechanisms and intermediate involved in the advanced azo dye degradation for industrial applications. *Journal of Molecular Structure*, **1224**, 129195.

4. Kaur, H., Kumar, S., Verma, N. K. & Singh, P. (2018) Role of pH on the photocatalytic activity of TiO_2 tailored by W/T mole ratio. *Journal of Materials Science: Materials in Electronics*, **29(18)**, 16120-16135.

5. Ma, D., Yi, H., Lai, C., Lai, C., Huo, X., An, Z., Li, L., Fu, Y., Li, B., Zhang, M., Qin, L., Liu, S. & Yang, L. (2021) Critical review of advanced oxidation processes in organic wastewater treatment. *Chemosphere*, **275**, 130104.

6. Mishra, S. & Sundaram, B. (2023) A review of the photocatalysis process used for wastewater treatment. *Materials Today: Proceedings*, **102**.

7. Garcia-Segura, S. & Brillas, E. (2017) Applied photoelectrocatalysis on the degradation of organic pollutants in wastewaters. *Journal of Photochemistry and Photobiology C-photochemistry Reviews*, **31**, 1–35.

8. Rao, P. A. & Satyanarayana, S. V. (2022) Improvement in photocatalytic activity of titanium dioxide nanoparticles through doping and calcination for textile wastewater treatment under visible light. *Materials Today: Proceedings*, **57**, 1918-1923.

9. Wudil, Y., Ahmad, U. F., Gondal, M. A., Al-Osta, M. A., Almohammedi, A., Sa'id, R., Hrahsheh, F., Haruna, K. & Mohamed, M. (2023) Tuning of graphitic carbon nitride (g-C_3N_4) for photocatalysis: A critical review. *Arabian Journal of Chemistry*, **16(3)**, 104542.

10. Vijayan, M., Manikandan, V., Rajkumar, C., Hatamleh, A. A., Alnafisi, B. K., Easwaran, G., Liu, X., Sivakumar, K. & Kim, H. (2022) Constructing Z-scheme g-C_3N_4/TiO_2 heterostructure for promoting degradation of the hazardous dye pollutants. *Chemosphere*, **311**, 136928.

11. Zhao, S., Lu, R., Yang, Y., Lu, Y., Rodriguez, R. D. & Chen, J. (2023) Direct Z-scheme g-C_3N_4/TiO_2 heterojunction porous nanotubes: An ingenious synthesis strategy to enhance photocatalytic activity. *Journal of Environmental Chemical Engineering*, **11(2)**, 109366.

12. Saeed, M., Asghar, H., Khan, I., Akram, N. & Usman, M. (2024) Synthesis of TiO_2-g-C_3N_4 for efficient photocatalytic degradation of Congo red dye. *Catalysis Today*, **447**, 115154–115154.

13. De Melo Oliveira, A. C., De Jesus, R. A., Bilal, M., Iqbal, H. M., Bharagava, R. N., Yerga, R. M., Ferreira, L. F. R., Egues, S. M. & Figueiredo, R. T. (2022) Influence of sound and calcination temperature on the fabrication of TiO_2-based photocatalysts and their photoactivity for H_2 production. *Molecular Catalysis*, **529**, 112523.

14. Jiang, W., Zhang, X., Gong, X., Yan, F. & Zhang, Z. (2010) Sonochemical synthesis and characterization of magnetic separable Fe_3O_4–TiO_2 nanocomposites and their catalytic properties. *International Journal of Smart and Nano Materials*, **1(4)**, 278–287.

15. Katta, K. & Dubey, R. (2020) Comparative study of doped-TiO_2 nanocrystals prepared by sol-gel and solvothermal approaches. *Materials Today Proceedings*, **39**, 1422–1425.

16. Imbar, A., Kumar, V. V. & Mamane, H. (2022) Solvothermal Synthesis of g-C_3N_4/TiO_2 Hybrid Photocatalyst with a Broaden Activation Spectrum. *Catalysts*, **13(1)**, 46.

17. Fu, M., Pi, J., Dong, F., Duan, Q. & Guo, H. (2013) A Cost-Effective Solid-State Approach to Synthesize g-C_3N_4 Coated TiO_2 Nanocomposites with Enhanced Visible Light Photocatalytic Activity. *International Journal of Photoenergy*, **2013**, 1–7.

18. Fagan, R., McCormack, D. E., Hinder, S. J. & Pillai, S. D. (2016) Photocatalytic Properties of g-C_3N_4–TiO_2 Heterojunctions under UV and Visible Light Conditions. *Materials*, **9(4)**, 286.

19. Albiter, E., Valenzuela, M. A., Alfaro, S., Valverde-Aguilar, G. & Martínez-Pallares, F. (2015) Photocatalytic deposition of Ag nanoparticles on TiO_2: Metal precursor effect on the structural and photoactivity properties. *Journal of Saudi Chemical Society*, **19(5)**, 563–573.

20. Ratshiedana, R., Mafa, P. J., Fakayode, O. J., Mishra, A. K. & Kuvarega, A. T. (2024) Ag doped TiO_2 anchored on metal free g-C_3N_4 for enhanced solar light activated photodegradation of a dye. *Optical Materials*, **157**, 116125.

21. Gan, W., Fu, X., Guo, J., Zhang, M., Li, D., Ding, C., Lu, Y., Wang, P. & Sun, Z. (2022) Ag nanoparticles decorated 2D/2D TiO_2/g-C_3N_4 heterojunction for efficient removal of tetracycline hydrochloride: Synthesis, degradation pathways, and mechanism. *Applied Surface Science*, **606**, 154837–154837.

22. Abdul Ghani, N. I., Zanal, N. I. N., Md Natar, N. S., Hamzah, S. R., Rosli, M. A., Muhamad, N. A., Mohd Azami, M. S., Mohamad, S. & Ismail, W. I. N. W. (2024) Ag-doped TiO_2 with tuneable Ag^0 and Ag^+ for enhanced photocatalytic degradation of RR4 dye. *Malaysian Journal of Chemistry*, **26(2)**, 12–26.

23. Nagaraj, G., Brundha, D., Chandraleka, C., Arulpriya, M., Kowsalya, V., Sangavi, S., Jayalakshmi, R., Tamilarasu, S. & Murugan, R. (2020) Facile synthesis of improved anatase TiO_2 nanoparticles for enhanced solar-light driven photocatalyst. *SN Applied Sciences*, **2(4)**.

24. Azizi-Toupkanloo, H., Karimi-Nazarabad, M., Shakeri, M. & Eftekhari, M. (2019) Photocatalytic mineralization of hard-degradable morphine by visible light-driven Ag@g-C_3N_4 nanostructures. *Environmental Science and Pollution Research*, **26(30)**, 30941–30953.

25. Matias, M. L., Reis-Machado, A. S., Rodrigues, J., Calmeiro, T., Deuermeier, J., Pimentel, A., Fortunato, E., Martins, R. & Nunes, D. (2023) Microwave synthesis of visible-light-activated g-C_3N_4/TiO_2 photocatalysts. *Nanomaterials*, **13(6).**

26. Rocha, M., Pereira, C. & Freire, C. (2021) Au/Ag nanoparticles-decorated TiO_2 with enhanced catalytic activity for nitroarenes reduction. *Colloids and Surfaces A: Physicochemical and Engineering Aspects*, **621**, 126614.

27. Moradi, A., Kazemeini, M., Hosseinpour, V. & Pourebrahimi, S. (2024) Efficient degradation of naproxen in wastewater using Ag-deposited ZnO nanoparticles anchored on a house-of-cards-like MFI-type zeolite: Preparation and physicochemical evaluations of the photocatalyst. *Journal of Water Process Engineering*, **60**, 105155.

28. Prymak, O., Jakobi, J., Rehbock, C., Epple, M. & Barcikowski, S. (2018) Crystallographic characterization of laser-generated, polymer-stabilized 4 nm silver-gold alloyed nanoparticles. *Materials Chemistry and Physics*, **207**, 442–450.

29. Hossain, M. S. & Ahmed, S. (2023) Easy and green synthesis of TiO_2 (Anatase and Rutile): Estimation of crystallite size using Scherrer equation, Williamson-Hall plot, Monshi-Scherrer Model, size-strain plot, Halder- Wagner Model. *Results in Materials*, **20**, 100492.

30. Wang, M., Zeng, Y., Dong, G. & Wang, C. (2020) Br-doping of g-C_3N_4 towards enhanced photo-catalytic performance in Cr(VI) reduction. *Chinese Journal of Catalysis*, **41(10)**, 1498–1510.

31. Moradi, S., Isari, A. A., Hayati, F., Rezaei Kalantary, R. & Kakavandi, B. (2021) Co-implanting of TiO_2 and liquid-phase-delaminated g-C_3N_4 on multi-functional graphene nanobridges for enhancing photocatalytic degradation of acetaminophen. *Chemical Engineering Journal*, **414**, 128618.

32. Fu, N., Chen, H., Chen, R., Ding, S. & Ren, X. (2023) Effect of calcination temperature on the structure, crystallinity, and photocatalytic activity of core-shell SiO_2@TiO_2 and mesoporous hollow TiO_2 composites. *Coatings*, **13(5)**.

33. Adzis, N. S., Suhaimi, N. H. S., Abdul Ghani, N. I., Abd Yami, N. F. N., Muhamad, N. A., Mohd Azami, M. S. & Nawawi, W. I. (2023) Modification of silver oxide/silver doped titanium dioxide (Ag_2O/Ag-TiO_2) photocatalyst using an immobilized reverse photodeposition method for photodegradation of Reactive Red 4 Dye. *Malaysian Journal of Chemistry*, **25(4)**.

34. Pacorel, V., Berger, P., Moutarlier, V., Marco de Lucas, M. del C., Montesin, T., Geoffroy, N., Herbst, F., Heintz, O., Optasanu, V. & Lavisse, L. (2024) Quantification and kinetics of nitrogen mass gain during high temperature oxidation of titanium in air. *Corrosion Science*, **234**, 112137.

35. Pop, O. L., Mesaros, A., Vodnar, D. C., Suharoschi, R., Tăbăran, F., Mageruşan, L., Tódor, I. S., Diaconeasa, Z., Balint, A., Ciontea, L. & Socaciu, C. (2020) Cerium oxide nanoparticles and their efficient antibacterial application in vitro against gram-positive and gram-negative pathogens. *Nanomaterials (Basel)*, **10(8)**.

36. Lu, C. & Zhou, H. (2022) The Ag-based SPR effect drives effective degradation of organic pollutants by BiOCOOH/AgBr composites. *Advanced Powder Technology*, **33(3)**, 103428.

37. Choudhary, S., Sooraj, K. P., Ranjan, M. & Mohapatra, S. (2024) Facile synthesis, morphological, optical, catalytic and photocatalytic properties of Ag nanoparticles decorated Ce doped ZnO hybrid plasmonic nanorods. *Inorganic Chemistry Communications*, **169**, 113008.

38. Jaafar, N. F., Jalil, A. A., Triwahyono, S., Efendi, J., Mukti, R. R., Jusoh, R., Jusoh, N. W. C., Karim, A. H., Salleh, N. F. M. & Suendo, V. (2015)

Direct in situ activation of Ag^0 nanoparticles in synthesis of Ag/TiO_2 and its photoactivity. *Applied Surface Science*, **338**, 75–84.

39. Gogoi, D., Namdeo, A., Golder, A. K. & Peela, N. R. (2020) Ag-doped TiO_2 photocatalysts with effective charge transfer for highly efficient hydrogen production through water splitting. *International Journal of Hydrogen Energy*, **45(4)**, 2729–2744.

40. Abdul Ghani, N. I., Rosli, M. A., Hamzah, S. R., Natar, N. S., Nazeri, N. S., Ab Aziz, S. I., Mohamad, S., Suhaimi, N. H. S., Adzis, N. S., Mohd Azami, M. S. & Nawawi, W. I. (2022) Water-based Immobilized Ag-doped TiO_2 photocatalyst for photocatalytic degradation of RR4 Dye. *Science Letters*, **16(2)**, 24–39.

41. Cao, W., Lin, K., Li, J., Qiu, L., Dong, Y., Wang, J., Xia, D., Fan, R. & Yang, Y. (2019) Iodine-doped graphite carbon nitride for enhancing photovoltaic device performance via passivation trap states of triple cation perovskite films [10.1039/C9TC04264D]. *Journal of Materials Chemistry C*, **7(40)**, 12717–12724.

42. Gkini, K., Martinaiou, I. & Falaras, P. (2021) A review on emerging efficient and stable perovskite solar cells based on g-C_3N_4 nanostructures. *Materials*, **14(7)**, 1679.

43. Matias, M. L., Morais, M., Pimentel, A., Vasconcelos, F. X., Reis Machado, A. S., Rodrigues, J., Fortunato, E., Martins, R. & Nunes, D. (2022) Floating TiO_2-cork nano-photocatalysts for water purification using sunlight. *Sustainability*, **14(15)**.

44. Hassan, F., Bonnet, P., Dangwang Dikdim, J. M., Gatcha Bandjoun, N., Caperaa, C., Dalhatou, S., Kane, A. & Zeghioud, H. (2022) Synthesis and investigation of TiO_2/g-C_3N_4 performance for photocatalytic degradation of bromophenol blue and eriochrome black T: Experimental design optimization and reactive oxygen species contribution. *Water*, **14(20)**.

45. Liang, S. -X., Zhang, L. -C., Reichenberger, S. & Barcikowski, S. (2021) Design and perspective of amorphous metal nanoparticles from laser synthesis and processing. *Physical Chemistry Chemical Physics*, **23(19)**, 11121–11154.

46. Aziz, S. B., Abdulwahid, R. T., Rasheed, M. A., Abdullah, O. G. & Ahmed, H. M. (2017) Polymer blending as a novel approach for tuning the SPR peaks of silver nanoparticles. *Polymers (Basel)*, **9(10)**.

47. Li, L., Zhao, H., Wang, X. & Guo, L. (2024) Recent advances of amorphous nanomaterials: Synthesis and applications. *Chinese Journal of Chemistry*, **42(22)**, 2853–2876.

48. Chen, D., Wang, K., Xiang, D., Zong, R., Yao, W. & Zhu, Y. (2014) Significantly enhancement of photocatalytic performances via core–shell structure of ZnO@mpg-C_3N_4. *Applied Catalysis B: Environmental*, **147**, 554–561.

49. Wang, Q., Li, Y., Huang, F., Song, S., Ai, G., Xin, X., Zhao, B., Zheng, Y. & Zhang, Z. (2023) Recent advances in g-C_3N_4-based materials and their application in energy and environmental sustainability. *Molecules*, **28(1)**.

50. Narkbuakaew, T., Sattayaporn, S., Saito, N. & Sujaridworakun, P. (2022) Investigation of the Ag species and synergy of Ag-TiO_2 and g-C_3N_4 for the enhancement of photocatalytic activity under UV–Visible light irradiation. *Applied Surface Science*, **573**, 151617.

51. Gao, J., Deng, J., Wang, Y., Liu, M., Zheng, L., Li, Y., Wang, Y., Chen, C., He, G. & Liu, Y. (2023) Multifunctional TiO_2/g-C_3N_4/Ag nanorod array film as a powerful substrate for surface-enhanced Raman scattering detection and green degradation. *Ceramics International*, **49(9, Part A)**, 13548–13558.

52. Xu, J. & Ma, S. (2023) High-efficiency photocatalytic degradation of RhB by protonation of g-C_3N_4 with Ag-loaded TiO_2 nanofibers. *Journal of Crystal Growth*, **617**, 127290.

53. Ratshiedana, R., Mafa, P. J., Fakayode, O. J., Mishra, A. K. & Kuvarega, A. T. (2024) Ag doped TiO_2 anchored on metal free g-C_3N_4 for enhanced solar light activated photodegradation of a dye. *Optical Materials*, **157**, 116125.